

RSC Advances



This is an *Accepted Manuscript*, which has been through the Royal Society of Chemistry peer review process and has been accepted for publication.

Accepted Manuscripts are published online shortly after acceptance, before technical editing, formatting and proof reading. Using this free service, authors can make their results available to the community, in citable form, before we publish the edited article. This *Accepted Manuscript* will be replaced by the edited, formatted and paginated article as soon as this is available.

You can find more information about *Accepted Manuscripts* in the [Information for Authors](#).

Please note that technical editing may introduce minor changes to the text and/or graphics, which may alter content. The journal's standard [Terms & Conditions](#) and the [Ethical guidelines](#) still apply. In no event shall the Royal Society of Chemistry be held responsible for any errors or omissions in this *Accepted Manuscript* or any consequences arising from the use of any information it contains.

The Importance of Crystallographic Texture in the Use of Titanium as an Orthopedic Biomaterial

Sumit Bahl, Satyam Suwas, Kaushik Chatterjee*

Department of Materials Engineering, Indian Institute of Science, Bangalore, India 560012

* Corresponding author: kchatterjee@materials.iisc.ernet.in; +91-80-22933408

Abstract

Crystallographic texture is perceived to play an important role in controlling material properties. However, the influence of texture in modulating the properties of biomedical materials has not been well investigated. In this work, commercially pure Titanium (cp-Ti) was processed through six different routes to generate a variety of textures. The effect of texture on mechanical properties, corrosion behavior, cell proliferation and osteogenesis was characterized for potential use in orthopedic applications. The presence of close-packed, low-energy crystallographic planes at the material surface was influenced by the volume fraction of texture components in the overall texture thereby influencing surface energy and corrosion behavior. Texture modulated osteoblast proliferation through differences in surface water-wettability. It also affected mineralization by possibly influencing the coherency between the substrate and calcium phosphate deposits. This study demonstrates that crystallographic texture can be an important tool in improving the properties of biomaterials to achieve enhanced performance of biomedical implants.

Keywords: Titanium; Orthopedics; Crystallographic texture; Biomaterials

1. Introduction

Bone tissues play an important role of providing structure and support to the human body. Bones articulate in the body at many places through the cartilage tissue to facilitate movement of joints. Cartilage is incapable of regenerating itself unlike bone and wears out with age. This type of degenerative disease is commonly described as osteoarthritis (OA). OA also arises from sport injuries and obesity¹. The most common treatment of OA is the use of orthopedic implants and the global market is projected to be worth 46 billion US dollars by 2017². With increasing cases of OA in younger population, it is desired that the durability of these implants be significantly longer than the current generation of implants which typically last no more than 15 years. This would minimize implant failure thereby eliminating the need for repeated surgeries in an individual's lifetime.

The implants being currently used clinically are made of Titanium and its alloys, stainless steel and Co-Cr alloys. Titanium and its alloys are the best in class materials for orthopedic applications because of low cytotoxicity, higher specific strength, lower elastic modulus, and excellent corrosion resistance. But a significant fraction of these devices fail in the body due to poor adhesion with bone (osseointegration), stress shielding due to mismatch of the elastic modulus, fatigue, corrosion fatigue, fretting, inflammation caused by wear debris and toxicity induced by the release of metal ions such as aluminum and vanadium³⁻¹¹. Therefore, newer alloy compositions are being developed with bioactive surface properties, lower elastic modulus, superior mechanical properties, higher wear resistance and non-toxic alloying elements¹². Aside from changing the material composition, the control of crystallographic texture offers an alternative route to improving many of these material properties.

Texture of a polycrystalline material can be defined as distribution of orientations of constituent grains inside the material¹³. The properties of polycrystalline materials are governed

by individual crystals as well as their orientation distribution within the material. When all possible orientations of a crystal are present with equal probability, the material is said to have a random texture. A random texture will yield an isotropic material due to averaging of properties in all directions. However, often anisotropy in properties may be desirable. This can be achieved by developing a non-random texture in materials. Texture in sheet materials is defined as $(hkl)[uvw]$, where (hkl) is the plane parallel to rolling plane and $[uvw]$ is the direction parallel to rolling direction. Titanium and alloys are known to develop acicular and equiaxed microstructures depending upon their heat treatments. Such treatments can further modify their crystallographic texture. In general, the texture of titanium is characterized by the disposition of c-axes (or basal poles) of hexagonal crystals in the pole figure. For example, cold rolled Titanium is known to display a texture where the c-axes are tilted by 25° from normal direction (ND) of the sheet towards the transverse direction (TD). Texture has been widely used to modulate the properties of Titanium alloys^{14, 15}.

The use of crystallographic texture to modulate properties of biomaterials has been largely ignored. Texture can influence both bulk and surface properties in materials and thus has the potential to significantly affect biomaterial performance. An inverse correlation exists between planar atomic density and surface energy. It is reported that surface energies of (0002) , $(10\bar{1}0)$ and $(11\bar{2}0)$ in Ti are 988 ergs/cm², 1049 ergs/cm², 1132 ergs/cm², respectively¹⁶. The basal planes in a hexagonal crystal have lowest surface energy due to highest planar atomic density. The orientation of basal poles with respect to material surface can, therefore, affect the surface energy of the material-biology interface. This can have manifestation in surface-dependent phenomena such as corrosion, wettability, and cell-material interactions. A few studies have reported the effect of texture on cell response^{17, 18}. Faghihi et al reported that grain orientation in polycrystalline Ti-6Al-4V alloy can affect its interactions with osteoblasts owing

to differences in surface energy^{17, 18}. In a recent study, Hoseini et al reported that texture and not grain size influences cell attachment to Ti surfaces^{17, 18}. However, a comprehensive study elucidating the structure-property-processing relationships essential to demonstrate the importance of texture in biomaterials science is hitherto unreported. As a model system, in this work, commercially pure Ti (cp-Ti) was processed by rolling through various routes to generate different textures. The developed textures varied in orientations and volume fractions of basal planes with respect to the surface. The processing routes were designed to produce similar microstructures but different texture to exclusively study the effect of texture. The effects of texture on mechanical properties, corrosion resistance, and osteoblast proliferation and mineralization were demonstrated.

2. Materials and Methods

2.1. Material and Processing

cp-Ti pan cakes (100 mm diameter x 14 mm thickness) in as-cast condition were a kind gift from the Defense Metallurgical Research Laboratory, Hyderabad, India. Rectangular samples cut from the pan cakes were homogenized at 1000 °C for 1 h. The samples were subsequently hot rolled at 1000 °C to a thickness of 10 mm in order break down the cast microstructure. These samples were used for all the further processing. The initial hot rolled plates were further rolled down to a thickness of 2 mm (true strain, $\epsilon_t=1.6$) through six different routes which are summarized in Figure 1. The plates were hot rolled in β phase at 1000 °C (hereafter designated as HR1000) and in α phase at 800 °C (HR800) with $\epsilon_t=0.1$ per pass resulting in total 16 passes to obtain a 2 mm thick sheet. The plates were uni-directionally rolled (UDR) and multi-step cross-rolled (MSCR) at 30 °C with $\epsilon_t=0.02$ per pass resulting in a total of 80 passes to a final thickness of 2 mm. Note that in the case of UDR, the sample direction was not changed in between the passes whereas in the case of MSCR the sample was rotated by 90° in the plane of sheet after every pass. The UDR and MSCR plates were cut into half and one half was further annealed at 750 °C for 1 h (UDR+A and MSCR+A, respectively) to generate annealed microstructures. All the samples were coated with Delta glaze before placing in the furnace to prevent formation of alpha casing.

2.2. Microstructure

Microstructure was characterized on a plane perpendicular to transverse direction (TD) of the rolled sheet. The samples were polished up to P3000 paper followed by electropolishing at 38 V for 20 s in A3 solution using Struers Lectropol-5. The samples were etched by immersing in

Kroll's reagent for 20 s followed by washing in fresh water. Micrographs were obtained using an optical microscope (Zeiss).

2.3. X-Ray Texture and Electron Backscatter Diffraction

X-Ray diffraction profiles of the samples were measured using Cu-K α radiation at a scan speed of 0.016 °/s (PanAnalytical X'pert Pro). Bulk texture of the samples was measured by X-ray texture goniometer (Bruker D8 Discover) in Schulz reflection geometry using Cu K α radiations. Six pole figures (10.0), (00.2), (10.1), (10.2), (11.0) and (10.3) were measured with a 2.5° x 2.5° grid size and 3 s per step. The samples were oscillated in x and y directions with 1 mm amplitude and 1 mm/s speed. The data from these pole figures was used to calculate orientation distribution function using commercially available LaboTex software (LaboSoft s.c., Krakow, Poland). These ODF's were used to generate complete (0002) pole figure for texture analysis.

Electron backscatter diffraction (EBSD) was performed on HR800, UDR+A and MSCR+A. Samples were polished as described above. EBSD scans were performed in ESEM-Quanta equipped with an EBSD detector (TexSEM Laboratories, Draper, UT) at 25 kV, 5.0 spot size, 13 mm working distance and step size of 2 μ m. Analysis of the data was done using commercially available TSL-OIM version 5.2 software (EDAX Inc., Mahwah, NJ).

2.4. Mechanical Properties

Uni-axial tensile tests (Instron 5967 universal testing machine with a 5 kN load cell) were performed such that the rolling direction of the sample was parallel to the tensile axis. The tests were performed until fracture at a strain rate of 10^{-3} s $^{-1}$.

2.5. Electrochemical Behavior

Corrosion behavior of disc-shaped samples (10 x mm diameter X 2 mm thickness) was evaluated by potentiodynamic polarization in simulated body fluid (SBF) of the following composition: 8.0 g/L NaCl, 0.35 g/L NaHCO₃, 0.224 g/L KCl, 0.228 g/L K₂HPO₄·3H₂O, 0.30 g/L MgCl₂·6H₂O, 40 mL/L 1M HCl, 0.278 g/L CaCl₂, 0.071 g/L Na₂SO₄, 6.0 g/L (CH₂OH)₃CHN₂¹⁹. Samples were electropolished as above. A three electrode potentiostat (Gill AC) was used with Pt as counter electrode and saturated calomel electrode (SCE) as reference. Samples were immersed in SBF for 3 h prior to polarization to stabilize the rest potential (open circuit potential, OCP). Polarization was performed from -200 mV to +1000 mV with respect to OCP at a rate of 12 mV/min. Corrosion potential (E_{corr}) and corrosion current density (I_{corr}) were calculated by Tafel extrapolation technique.

2.6. Water Contact Angle

Static contact angle of ultrapure water (Sartorius Arium) was measured using a goniometer (OCA 15EC, Dataphysics) on the surface of samples prepared by electropolishing. Contact angle was measured after placing 1 μl of water droplet on the sample. Three replicates of each sample were tested for statistical analysis.

2.7. Cell Proliferation and Osteogenesis

Biological response of the samples was evaluated in vitro using MC3T3-E1 subclone 4 cell line (ATCC), which is a well-established osteoblast model²⁰. The cells were cultured in α -Minimum Essential Medium (α -MEM) supplemented with 10 % (v/v) fetal bovine serum (FBS, Gibco, Life Technologies), as reported previously²¹. Penicillin-streptomycin (Sigma-Aldrich) antibiotic was also added to the culture media at 1 % (v/v) concentration. Trypsin-EDTA was used to passage the cells which were subsequently sub-cultured. Passage 3 cells were used for all studies reported herein. Samples (square cross-section of 4 mm x 4 mm and 2 mm thickness) for

cell studies were cut using an electro-discharge machine (EDM, Accutex). All samples were electropolished and sterilized by immersing in ethanol for 30 min followed by exposure to UV for 1 h prior to seeding cells. Samples were placed individually in wells of 96-well tissue culture polystyrene (TCPS) plate. 200 μL of cell suspension containing 5×10^3 cells was added to each well. Cell attachment and proliferation was characterized at 1 d and 3 d after seeding, respectively. MTT assay was used as quantitative measure of viable cells. Fluorescently-labeled cells were imaged to characterize cell morphology. Six replicates ($n = 6$) of each sample were used for each time interval; four replicates for the assay and two for imaging.

A stock solution of MTT dye (3-[4,5-dimethylthiazol-2-yl]-2,5-diphenyltetrazolium bromide; thiazolyl blue) (Sigma Aldrich) was prepared by dissolving MTT powder in sterile phosphate buffer saline (PBS) at a concentration of 5 mg/mL. Working solution of MTT was prepared by diluting the stock solution in fresh complete culture medium to a final concentration of 1 mg/mL. The cell culture medium was replaced with 100 μL of working solution and incubated at 37 °C and 5 % CO_2 for 3 h. In this assay the dye is reduced to formazon crystals by dehydrogenase enzyme produced in the mitochondria of viable cells. The crystals were dissolved in 75 μL of dimethyl sulphoxide (DMSO). Absorbance of the solution was measured at 570 nm using a micro-well plate reader (BioTek).

Cells were fixed using 3.7 % formaldehyde at 37 °C for 15 min. The cells were subsequently permeabilized with 0.2 % Triton X (Sigma Aldrich). Actin filaments were stained using 25 $\mu\text{g}/\text{mL}$ Alexa Fluor 546 (Invitrogen) at 37 °C for 15 min. Cell nuclei were stained using 0.2 $\mu\text{g}/\text{mL}$ DAPI (Invitrogen) at 37 °C for 5 min. Stained cells were imaged with an inverted fluorescence microscope (Olympus).

Osteogenesis was evaluated by measuring the amount of mineral deposits on the sample surfaces by cells cultured in osteogenic differentiation media. Osteogenic media was prepared by

adding β -glycerophosphate (10 mM) and ascorbic acid (50 $\mu\text{g}/\text{mL}$) to α -MEM. 200 μL of cell suspension in growth medium containing 5×10^3 cells was added to each well, as above. 24 h after seeding, media was replaced with osteogenic media. Media was replenished every 3 d. Mineral deposits were stained at 7 d using Alizarin Red S dye. Cells were fixed with 3.7 % HCHO at 37 $^{\circ}\text{C}$ for 20 min. Cells were subsequently stained with 1 % (wt/vol) Alizarin Red S solution at 37 $^{\circ}\text{C}$ for 30 min. The dye was removed and samples were washed with water for several times to remove unbound dye. The dye was dissolved in 150 μL solution of 0.5 N HCl and 5 % SDS at 37 $^{\circ}\text{C}$ for 30 min. Absorbance of the solution at 405 nm was measured in a micro-well plate reader (Biotek). Fourier Transformed Infrared Spectroscopy (FTIR, Perkin Elmer Spectrometer Frontier) was measured from 600 cm^{-1} to 4000 cm^{-1} to confirm the chemical nature of mineral deposits.

2.8. Statistical analysis

Analysis of Variance (ANOVA) with Tukey's test was used for all statistical analyses. Differences were considered significant at $p < 0.05$.

3. Results and Discussion

3.1. Microstructure and Texture

The processing schedules were designed in a manner so as to generate similar microstructures with different textures. The textures varied in terms of position of basal planes with respect to the surface and their intensities. This enabled the study of the effect of texture on material properties exclusively. UDR and MSCR are two variations of cold deformation which are known to produce different textures with similar microstructures²²⁻²⁵. Annealing of these two microstructures led to formation of UDR+A and MSCR+A respectively, with recrystallized microstructures, however with possible variation in texture. HR800 was also expected to give a recrystallized microstructure produced by dynamic recrystallization during hot rolling in α phase. Thus, HR800, UDR+A and MSCR+A could likely be three routes with similar microstructures but varying textures. HR1000 was expected to generate a transformation microstructure as the rolling was done above the β phase transformation temperature of 882 °C. The deformation was performed in a total of sixteen passes in order to generate a very weak texture with transformation microstructure.

3.1.1. Microstructural Characterization

Representative optical micrographs of the samples processed by the different routes are compiled in Figure 2. The HR1000 sample exhibits a typical transformation microstructure caused by the allotropic transformation from β to α phase on cooling below the transformation temperature of 880 °C. The microstructure is a combination of basket weave-like α as evident in the image, which is a result of fast air cooling from the rolling temperature²⁶. The average α colony size is 10 μm . Average grain misorientations in recrystallized HR800, UDR+A and MSCR+A samples were calculated from EBSD data to compare their state of recrystallization.

The grain misorientation angle was classified into three ranges: low angle 2° - 5° , medium angle 5° - 15° , and high angle 15° - 180° . The respective values for the three samples are summarized in Table 1. The microstructure of HR800 sample is dynamically partially recrystallized (Figure 2). Some grains in the microstructure are equiaxed while some are elongated due to multi-pass rolling. This can also be observed in the EBSD micrograph of HR800 (Figure 3). HR800 has a significantly high volume fraction of low angle boundaries due to presence of subgrains formed in dynamically partially recrystallized microstructure. The average grain size for HR800 is around $10\ \mu\text{m}$. Both UDR and MSCR show elongated grains characteristic of cold rolled samples (Figure 2). Their annealed counterparts, UDR+A and MSCR+A, exhibit completely recrystallized microstructure and are in the grain growth regime. The grains are equiaxed and majority of them ($> 80\%$) have high angle boundaries which is due to complete recrystallization. The average grain size for UDR+A and MSCR+A is $16\ \mu\text{m}$ and $15\ \mu\text{m}$, respectively.

3.1.2. Texture

The XRD profiles for the UDR and UDR+A samples are shown in Figure S1. The profiles confirm the crystal structure to be hexagonal closed packed in both cold rolled as well as annealed samples. There was no deformation induced phase transformation in the deformed samples. The (0002) basal pole figures of all the samples are shown in Figure 4. The positions of basal poles with respect to the normal direction (ND) are listed in Table 2. The volume fraction of basal fiber (0001)[uvw] was calculated from the orientation distribution function (ODF) with an orientation spread of 15° in three Euler's angles ϕ_1 , ϕ , ϕ_2 and is also listed in Table 2. In case of HR1000, transformation from β to α phase occurs through Burgers relationship, i.e., $(110)_{\beta} // (0001)_{\alpha}$ and $[111]_{\beta} // [11\bar{2}0]_{\alpha}$. There are 12 possible variants of the phase that can be generated after transformation due to symmetry of the parent cubic β phase. The texture developed in HR1000 samples is formed during the transformation from β to α phase on air

cooling. The texture obtained depends upon the texture of the β phase developed during hot rolling. In this present work, the basal poles are tilted by around 10° away from ND. The volume fraction of basal fiber is around 6 %. As desired, the overall texture developed is weak due to multiple pass deformation. The intermittent heating between passes would have resulted in nucleation of β grain from transformed α grain, which would again have transformed back to α after rolling. This process which was repeated after every pass likely led to the weakening of texture. Inagaki studied the transformation texture of cp-Ti and observed that multiple orientations are developed after transformation in cp-Ti²⁷. These are inherited from multiple orientations developed in the parent β phase during hot rolling as well as multiple variants from single β orientation. The α orientations derived from parent β orientation can have different intensities due to preferential selection of certain variants over others. As mentioned above, a possible reason for weaker textures in present work could be that the total deformation (80 %) was carried out in 16 passes whereas in the study by Inagaki's work the total deformation (94 %) was accomplished in 3 passes.

In the case of HR800, basal poles are tilted by 11° from ND towards TD. The volume fraction of basal fiber with 15° orientation spread in Euler's angles is 15 % which is very high compared to other conditions. The textures of UDR and MSCR are characterized by basal poles tilted by approximately 30° and 25° , respectively, away from ND and towards TD. The volume fraction of basal fiber for UDR and MSCR are 5.8 % and 4.6 %, respectively. The split of basal poles towards TD in UDR is typical of HCP metals with c/a ratio < 1.633 ²⁸. In MSCR samples, the split is both in RD and TD (can be named as RD1 and RD2) as the sample is rotated by 90° after every pass²². The major texture component $(11\bar{2}7)[1\bar{1}00]$ is same for both UDR and MSCR however, the texture is sharper for MSCR sample than UDR. This can be explained by the higher contribution of basal slip systems than prismatic and pyramidal systems in MSCR over UDR²².

Annealing of the cold deformed samples, UDR and MSCR at 750 °C led to complete recrystallization and further grain growth. The texture of UDR+A is sharpened significantly due to annealing. The basal poles are seen shifted farther apart from ND towards TD with a sharp intensity at 38° from ND as compared to 30° for UDR. The main texture component is 6° misoriented from $(10\bar{1}3)[1000]$ orientation. In the case of MSCR+A, the basal poles also shift further away from ND towards TD at 35° from ND. The increase in intensity of texture is less compared to UDR+A. The main orientation component is misoriented by approximately 6° from $(10\bar{1}3)[13\bar{4}1]$ orientation. The annealing textures of HCP materials in the grain growth regime are derived from primary recrystallization texture which is similar to cold rolled texture by a rotation 30° around the c-axis²⁹.

Analysis of texture revealed that UDR and MSCR samples have only subtle difference in texture. The texture of MSCR is stronger and its basal poles are closer to ND than UDR. Likewise, textures of UDR+A and MSCR+A are qualitatively similar. The strength of UDR+A texture is higher than MSCR+A. Thus, UDR/MSCR and UDR+A/MSCR+A form two sets with similar microstructure but textures of varying strengths. Also, HR800, UDR+A, and MSCR+A samples have similar recrystallized microstructures but significantly different texture.

3.2. Properties: Mechanical, Electrochemical, Wettability and Osteoblast Response

3.2.1. Mechanical Properties

Stress-strain curves of all the samples are plotted in supplementary Figure S2 and the values of yield strength (YS), ultimate tensile strength (UTS) and ductility are listed in Table 3. The cold rolled samples, UDR and MSCR, show highest strength and lowest ductility. They contain a very high dislocation density compared to the hot rolled and annealed samples leading to the highest strengths. Dislocation density of cold rolled samples reduces on annealing due to

recrystallization. As a result, UDR+A and MSCR+A samples have significantly lower strength and higher ductility than the cold rolled samples. In contrast, HR800 is dynamically partially recrystallized. A large volume fraction of low angle grain boundaries suggest the presence of subgrains and a higher dislocation density. Therefore HR800 has higher strength than UDR+A and MSCR+A with slightly lesser ductility. HR1000 has a higher strength than UDR+A and MSCR+A. It exhibits a transformation microstructure in which the strength is governed primarily by the size of individual α lath and α colony size. Misorientation between individual laths is low which will allow the dislocation to pass through them but still act as a barrier to their movement thereby leading to strengthening. On the other hand, movement of dislocations from one colony to another will likely be hindered due to higher misorientation leading to further strengthening. Strength is reported to increase with decrease in the sizes of both individual lath and colony^{30, 31}. Average colony size in HR1000 is around 10 μm , whereas the average grain size for UDR+A and MSCR+A are 15 μm and 16 μm , respectively. Higher strength of HR1000 than the annealed samples is therefore likely due to its smaller colony size and unique microstructure.

3.2.2. Surface Water Wettability

The water contact angle (θ) of the samples are listed in Table 2. The variation in contact angle scales with the deviation of basal planes from away from the surface. Water adhesion tension, $\tau^\circ = \gamma^\circ_{\text{IV}} \times \cos\theta$ is plotted against the deviation of basal poles from ND towards TD in Figure 5(a)³². γ° (72 dyne/cm) is the interfacial surface tension of pure water with air. A higher contact angle would lead to a lower τ° value. It can be seen that τ° varies linearly with the deviation of basal planes. τ° depends on the surface energy of substrate. A lower surface energy results in a lower τ° (higher contact angle) indicating increased hydrophobicity. As mentioned above, basal planes of HCP structure are closest packed and therefore, have the lowest surface

energy (988 erg/cm^2)¹⁶. Thus, increased presence of basal planes on the surface is likely to result in lower τ° . Texture analysis revealed that basal planes are closest to the surface for HR1000 and HR800, which is reflected in the lowest τ° values. In UDR+A and MSCR+A, the basal planes are farthest away from the surface and therefore result in higher τ° values. Vogler found that hydrophobic forces are ineffective on surfaces with τ° greater than 33.7 dyne/cm (contact angle = 62.4°). Both HR1000 and HR800 surfaces have τ° values less than 33.7 dyne/cm indicating hydrophobic nature³². On the other hand, τ° for UDR, MSCR, UDR+A and MSCR+A are higher than 33.7 dyne/cm indicating hydrophilic nature for these surfaces.

3.2.3. Electrochemical Properties

Potentiodynamic polarization plots of the samples measured in SBF are compiled in supplementary Figure S3. Corrosion current density values calculated by Tafel extrapolation method are listed in Table 4. It was observed that the HR1000 and HR800 samples have the lowest corrosion rates among all the different processing routes. Interestingly, the corrosion rates of UDR and MSCR were found to be lower than UDR+A and MSCR+A. This is in sharp contrast to the general belief that deformed microstructures exhibit higher corrosion rates than annealed microstructures due to higher grain boundary area and defect density in the former. This trend, however, is reportedly reversed when samples are subject to severe plastic deformation (SPD) such as equal channel angular pressing (ECAP) where nano-crystalline grains formed. These SPD samples are reported to exhibit better resistance than the unprocessed coarse grained samples^{33, 34}. The corrosion resistance improves with reduction in grain sizes. Homogeneous distribution of defects and impurities in the material due to severe deformation is argued to be the underlying cause of improved corrosion resistance. However, UDR and MSCR were not severely deformed but still these have better corrosion resistance than annealed microstructures. One of the possible reasons for such a behavior is the difference in texture

between the deformed and annealed conditions. It has been observed that corrosion behavior depends upon the crystallographic plane parallel to surface exposed to corrosion media³⁵. Planes which have higher atomic density show higher corrosion resistance due to their lower surface energy. Figure 5(b) presents the variation of corrosion rates with deviation of basal planes from ND towards TD. It can be seen that the corrosion rate scales linearly with the extent of deviation, irrespective of the microstructure. Presence of low energy (0002) basal planes parallel to the surface, thus, can lead to enhanced corrosion resistance. The basal poles shifted closer to ND away from TD in the deformed samples (Table 2). This likely negated the detrimental effect of deformation leading to increased corrosion resistance in the deformed samples (UDR and MSCR) compared to the annealed specimens (UDR+A and MSCR+A). HR800 is dynamic partially recrystallized and has corrosion rate lower than that of fully recrystallized UDR+A and MSCR+A. Corrosion rate of HR800 should have been similar to or slightly higher than UDR+A/MSCR+A due to the partial state of recrystallization. However, the basal planes are deviated by only 11° from the surface, whereas the deviation is more than 35° and 38° for MSCR+A and UDR+A respectively (Table 2). This likely resulted in lower corrosion rate of HR800 compared to UDR+A and MSCR+A. HR1000 was processed at the highest temperature where the parent β phase recrystallized and later transformed to α phase. Highest deformation temperature, recrystallized microstructure and presence of basal planes close to the surface (10° deviation) likely led to low corrosion rate observed for HR1000. The trend in corrosion rates elucidates the role of the low energy basal planes in determining the corrosion behavior and highlights the importance of crystallographic texture in such surface-dependent phenomena.

3.2.4. Osteoblast Proliferation and Osteogenesis

The potential effects of processing and texture of cp-Ti for orthopedic use on biological response was studied by measuring cell attachment and proliferation of mouse osteoblasts *in*

vitro. Figure 6 plots the absorbance values from the cell viability assay on the different samples. Initial attachment at 1 d was similar on all the samples except HR800 which was significantly ($p < 0.05$) lower compared to the other samples. Cell proliferation was evaluated by measuring cell viability at 3 d. Cells proliferated on all the surfaces evidenced by the increase in absorbance for all samples. However, statically-significant differences in the values at 3 d indicate that the cell proliferation was lower on HR1000 and HR800 than on the other four surfaces. Fluorescent images corroborated the results from the assay. Representative fluorescence images at 1 d and 3 d are shown in Figure 7 for HR800 and UDR+A. Cells were found to be equally well spread on all the samples. The cell numbers were observed to have increased on all the samples. Fewer cells were seen on HR800 than the other samples at 1 d. At 3 d, the differences between the different surfaces were less discernible visually as the cell proliferated to a nearly confluent monolayer.

The effect of surface on cellular behavior is modulated by the type and conformation of proteins adsorbed to the surface. Cell attachment and proliferation is reported to be dependent upon the wettability of surface mediated by protein adsorption events³⁶⁻³⁸. It has been found that hydrophilic surfaces facilitate binding of adhesive proteins such as vitronectin and fibronectin suitable for cell attachment and growth. Moreover, using theories of colloidal surface science, it was also shown that cell attachment and spreading is favored with increase in wettability of the biomaterial surface³⁹. In this study, osteoblast attachment and proliferation was lower on the relatively hydrophobic surfaces of HR1000 and HR800 compared to the other four surfaces which are hydrophilic as determined from measurement of the water adhesion tension (Figure 5a).

The effect of texture on early osteogenesis was measured at 7 d. The chemical composition of the mineral deposits was evaluated by FTIR spectroscopy. Representative FTIR

spectrum of the MSCR surface with mineral deposits is shown in supplementary Figure S4. Characteristic peak of phosphate group in the range of 1000 cm^{-1} to 1100 cm^{-1} along with a shoulder at 1077 cm^{-1} indicate deposition of calcium phosphate^{40, 41}. The absorbance values after dissolving the stained mineral deposits are compiled in Figure 8 for quantitative comparison. Osteoblasts on HR800 exhibited significantly ($p < 0.05$) higher mineral deposition compared to the other five surfaces. Mineral deposition on HR1000 was lower than HR800, but higher compared to the other surfaces which were not statistically different. It is known that the hydroxyapatite crystals in bone are highly oriented such that the normal to (0002) planes is parallel to axis of collagen fibrils⁴². Mao et al have shown that Ti substrate with (0002) texture led to oriented growth of HA through crystal matching between substrate and HA thereby mimicking the natural mineralization process⁴³. Both HR800 and HR1000 have the highest volume fraction of basal fiber and position of basal planes closest to the surface (Table 2). It is likely that highly oriented Ti substrate with (0002) parallel to its surface facilitated nucleation of oriented HA crystal. This in turn led to higher mineralization on HR800 and HR1000 samples.

Results of this study demonstrate that the choice of processing conditions can yield different microstructures and crystallographic textures in cp-Ti. This in turn can lead to significant differences in mechanical properties, corrosion resistance and osteoblast response. Table 5 summarizes the effects on the different properties. The semi-quantitative comparison indicates that texture affects strength, corrosion resistance and osteogenesis. HR800 offers the best combination of corrosion resistance, strength and osteogenesis among the library of processing routes studied herein. Properties of HR800 are closely matched by those of HR1000. Note that the effect of texture independent of microstructural changes can be elucidated by comparing HR800, UDR+A and MSCR+A, all of which have the same microstructure but

widely differing texture. It can be seen that HR800 exhibits significantly different properties than UDR+A and MSCR+A which can be attributed to differences in texture, as discussed above.

Surfaces of biomedical implants used in the clinical are often modified by hydroxyapatite (HA) coatings or surface roughening to improve osseointegration⁴⁴. Although not the focus of the current study, the surfaces obtained by these methods are also likely to be influenced by the texture of the underlying metal substrate in addition to the properties discussed in this study. Presence of (0002) planes of Ti were found to be better suited for biomimetic growth of HA coating^{43, 45}. In another study, osteoblast attachment, proliferation and osteogenesis were found to be higher on HA-coated Ti substrate with (0002) texture⁴⁶. Surface roughening treatments often performed with acid etching are also reported to depend on the texture. It not only affects surface roughness but also controls the planes exposed at the surface post treatment⁴⁷. Taken together, the results of this work and from previously reported studies elucidate the importance of texture in modulating bulk and surface properties of biomaterials both with or without surface treatments.

4. Conclusions

cp-Ti was processed through six different rolling routes to yield different crystallographic textures. Mechanical properties were determined by a combination of microstructure and texture. The availability of close-packed crystallographic planes and the resultant surface energy were determined by texture which in turn modulated corrosion rates, osteoblast proliferation and osteogenesis on the surface. The processing condition of HR800 offered the optimal combination of mechanical strength, corrosion resistance and osteogenesis. Taken together, this study exemplifies the importance of crystallographic texture in the use of metallic biomaterials and demonstrates that it can be an important tool to enhance their performance over and above that achieved through other means.

Acknowledgements

This work was funded by the Department of Atomic Energy- Board of Research in Nuclear Sciences (DAE-BRNS), India. K.C. gratefully acknowledges support through the Ramanujan fellowship from the Department of Science and Technology (DST), India. The authors acknowledge Defense Metallurgical Research Laboratory (DMRL, Hyderabad, India) for providing cp-Ti pan cakes. Authors thank Prof. Subodh Kumar and Mr. George Raphael for assistance with the corrosion studies and Mr. Sasidhara for assistance with tensile tests.

References

1. O. E. Union, *Health at a Glance: Europe 2010*, OECD Publishing.
2. *Orthopedic Implants – A Global Market Overview HC003*, 2011.
3. J. J. Jacobs, J. L. Gilbert and R. M. Urban, *J Bone Joint Surg Am*, 1998, **80**, 268-282.
4. D. F. Williams, Proc. Int. Symp. on Retrieval and Analysis of Orthopaedic Implants, 1977.
5. D. Hoepfner and V. Chandrasekaran, *Wear*, 1994, **173**, 189-197.
6. S. Steinemann, J. Eulenberger and P. Maesli, *Biological and biomechanical performance of biomaterials*, 1985, 409-414.
7. S. Cowin, W. Van Buskirk and R. Ashman, in *Handbook of Bioengineering*, eds. R. Skalak and S. Chien, McGraw-Hill, New York, 1987, pp. 2.1-2.27.
8. M. Wong, J. Eulenberger, R. Schenk and E. Hunziker, *J Biomed Mater Res*, 1995, **29**, 1567-1575.
9. L. Hong, X. Hengchang and K. De Groot, *J Biomed Mater Res*, 1992, **26**, 7-18.
10. R. Huiskes, *Acta Orthop Belg*, 1993, **59**, 118-129.
11. D. Puleo and A. Nanci, *Biomaterials*, 1999, **20**, 2311-2321.
12. M. Geetha, A. Singh, R. Asokamani and A. Gogia, *Prog Mater Sci*, 2009, **54**, 397-425.
13. S. Suwas and N. P. Gurao, *J Indian Inst Sci*, 2012, **88**, 151-177.
14. O. Kaibyshev, I. Kazachkov and R. Galeev, *J Materi Sci*, 1981, **16**, 2501-2506.
15. M. Peters, A. Gysler and G. Lütjering, *Metall Trans A*, 1984, **15**, 1597-1605.
16. M. Pascuet, R. Pasianot and A. Monti, *J Mol Catal A-Chem*, 2001, **167**, 165-170.
17. S. Faghihi, F. Azari, H. Li, M. R. Bateni, J. A. Szpunar, H. Vali and M. Tabrizian, *Biomaterials*, 2006, **27**, 3532-3539.

18. M. Hoseini, P. Bocher, A. Shahryari, F. Azari, J. A. Szpunar and H. Vali, *J Biomed Mater Res A*, 2013.
19. S. Bahl, S. Raj, S. Vanamali, S. Suwas and K. Chatterjee, *Mater Technol*, 2013, **29**, B64-B68.
20. H. Sudo, H.-A. Kodama, Y. Amagai, S. Yamamoto and S. Kasai, *The J. of Cell Biology*, 1983, **96**, 191-198.
21. K. Chatterjee, L. Sun, L. C. Chow, M. F. Young and C. G. Simon Jr, *Biomaterials*, 2011, **32**, 1361-1369.
22. N. Gurao, S. Sethuraman and S. Suwas, *Metall Mater Trans A*, 2013, **44**, 1497-1507.
23. N. P. Gurao, A. Ali A and S. Suwas, *Materials Science and Engineering: A*, 2009, **504**, 24-35.
24. S. Suwas, A. Singh, K. N. Rao and T. Singh, *Z Metallkd*, 2002, **93**, 918-927.
25. S. Suwas, A. Singh, K. N. Rao and T. Singh, *Z Metallkd*, 2002, **93**, 928-937.
26. S. Kim and J. Park, *Metall Mater Trans A*, 2002, **33**, 1051-1056.
27. H. Inagaki, *Z Metallkd*, 1990, **81**, 282-292.
28. H. Inagaki, *Z Metallkd*, 1991, **82**, 779-789.
29. H. Inagaki, *Z Metallkd*, 1992, **83**, 40-46.
30. G. Lütjering, *Materials Science and Engineering: A*, 1998, **243**, 32-45.
31. G. Yapici, I. Karaman, Z. Luo and H. Rack, *Scripta Mater*, 2003, **49**, 1021-1027.
32. E. A. Vogler, *Adv Colloid Interfac* 1998, **74**, 69-117.
33. A. Balakrishnan, B. Lee, T. Kim and B. Panigrahi, *Trends in Biomaterials and Artificial Organs*, 2008, **22**, 54-60.
34. A. Balyanov, J. Kutnyakova, N. Amirkhanova, V. Stolyarov, R. Valiev, X. Liao, Y. Zhao, Y. Jiang, H. Xu and T. Lowe, *Scripta Mater*, 2004, **51**, 225-229.

35. M. Hoseini, A. Shahryari, S. Omanovic and J. A. Szpunar, *Corros Sci*, 2009, **51**, 3064-3067.
36. C. J. Wilson, R. E. Clegg, D. I. Leavesley and M. J. Percy, *Tissue Eng*, 2005, **11**, 1-18.
37. J. G. Steele, C. McFarland, B. A. Dalton, G. Johnson, M. D. Evans, C. Rolfe Howlett and P. A. Underwood, *J Biomat Sci-Polym E*, 1994, **5**, 245-257.
38. T. J. Webster, C. Ergun, R. H. Doremus, R. W. Siegel and R. Bizios, *J Biomed Mater Res*, 2000, **51**, 475-483.
39. E. A. Vogler, *Biophys J*, 1988, **53**, 759-769.
40. S. Kumar, S. Bose and K. Chatterjee, *RSC Advances*, 2014, **4**, 19086-19098.
41. I. Mobasherpour, M. S. Heshajin, A. Kazemzadeh and M. Zakeri, *J Alloy Compd*, 2007, **430**, 330-333.
42. A. Veis, *The Chemistry and Biology of Mineralized Tissue*, Elsevier, Amsterdam, 1981, p. 617.
43. C. Mao, H. Li, F. Cui, C. Ma and Q. Feng, *J Cryst Growth*, 1999, **206**, 308-321.
44. L. Le Guéhennec, A. Soueidan, P. Layrolle and Y. Amouriq, *Dental materials*, 2007, **23**, 844-854.
45. C. Mao, H. Li, F. Cui, Q. Feng, H. Wang and C. Ma, *J. Mater. Chem.*, 1998, **8**, 2795-2801.
46. A. T. Rad, M. Novin, M. Solati-Hashjin, H. Vali and S. Faghihi, *Colloids and Surfaces B: Biointerfaces*, 2013, **103**, 200-208.
47. K. Sato, M. Shikida, T. Yamashiro, M. Tsunekawa and S. Ito, *Sensors and Actuators A: Physical*, 1999, **73**, 122-130.

Table 1. Grain misorientation angles and grain size for the hot rolled/annealed samples.

Processing	Grain misorientation angle (% volume fraction of grains)			Avg. grain size (μm)
	2°-5°	5°-15°	15°-180°	
HR800	52.9	16.5	30.7	10.0
UDR+A	5.4	13.1	81.5	16.0
MSCR+A	4.7	10.4	84.9	15.0

Table 2. Volume fraction of basal fiber, position of basal poles with respect to ND and major texture components of cp-Ti samples.

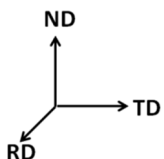
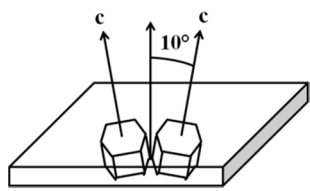
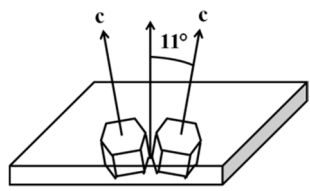
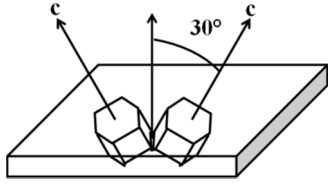
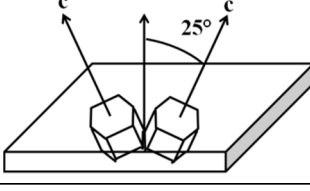
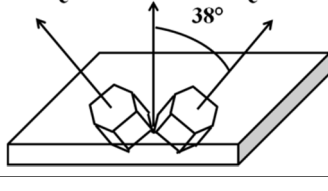
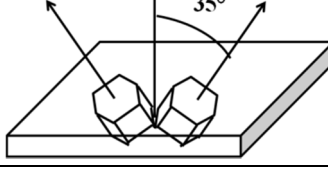
Sample	% Volume fraction Basal fiber (0002)[uvw]	Position of basal pole figure w.r.t. ND toward TD (°) 	Texture Component (hkl)[uvw]	Water Contact Angle (°) Mean ± S.D.
HR1000	6.0		(11 $\bar{2}$ 5)[1000], (10 $\bar{1}$ 8)[1000], (11 $\bar{2}$ 15)[1 $\bar{1}$ 00]	67.2 ± 1.7
HR800	15.0		(11 $\bar{2}$ 7)[1 $\bar{1}$ 00] (11 $\bar{2}$ 15)[1 $\bar{1}$ 00]	69.0 ± 5.0
UDR	5.8		(11 $\bar{2}$ 7)[1 $\bar{1}$ 00]	46.5 ± 1.5
MSCR	4.6		(11 $\bar{2}$ 7)[1 $\bar{1}$ 00]	55 ± 2.5
UDR+A	2.8		(10 $\bar{1}$ 3)[1000]	37.7 ± 2.8
MSCR+A	2.9		(10 $\bar{1}$ 3)[13 $\bar{4}$ 1]	43.8 ± 3.3

Table 3. Mechanical properties of cp-Ti samples

Sample	Yield Strength (MPa)	Ultimate Tensile Strength (MPa)	Ductility (%)
HR1000	495	570	39
HR800	635	683	38
UDR	787	828	26
MSCR	810	851	25
UDR+A	310	400	48
MSCR+A	311	400	44

Table 4. E_{corr} and I_{corr} values of cp-Ti samples in SBF calculated by Tafel extrapolation method.

Sample	E_{corr} (mV) vs. SCE	I_{corr} ($\times 10^{-5}$ mA/cm²)
HR1000	-347	2.45
HR800	-315	2.45
UDR	-368	2.95
MSCR	-323	3.00
UDR+A	-366	3.30
MSCR+A	-280	3.23

Table 5. Summary of the effects of processing of cp-Ti

Sample	Strength	Corrosion Resistance	Osteogenesis
HR1000	Medium	High	Medium
HR800	Medium	High	High
UDR	High	Medium	Low
MSCR	High	Medium	Low
UDR+A	Low	Low	Low
MSCR+A	Low	Low	Low

Figure captions

Figure 1. Flowchart illustrating the different processing routes of cp-Ti used in this study.

Figure 2. Optical micrographs of cp-Ti samples. Scale bar = 10 μm .

Figure 3. EBSD micrographs of hot rolled and annealed samples, along with the stereographic triangle. Scale bar = 200 μm .

Figure 4. (0002) pole figures of cp-Ti samples generated by X-ray texture measurements.

Figure 5. Plots of (a) water adhesion tension τ° and (b) corrosion rate I_{corr} , with deviation of basal pole from ND towards TD.

Figure 6. Absorbance values of cell viability assay at 1 d and 3 d. * and & indicate statistically significant difference ($p < 0.05$) at 1 d and 3 d, respectively.

Figure 7. Representative fluorescence micrographs at 1 d and 3 d. Scale bar = 100 μm

Figure 8. Absorbance values of dissolved dye bound to deposited mineral. *, & and # indicate statistically significant differences ($p < 0.05$) at 7d.

Figure 1

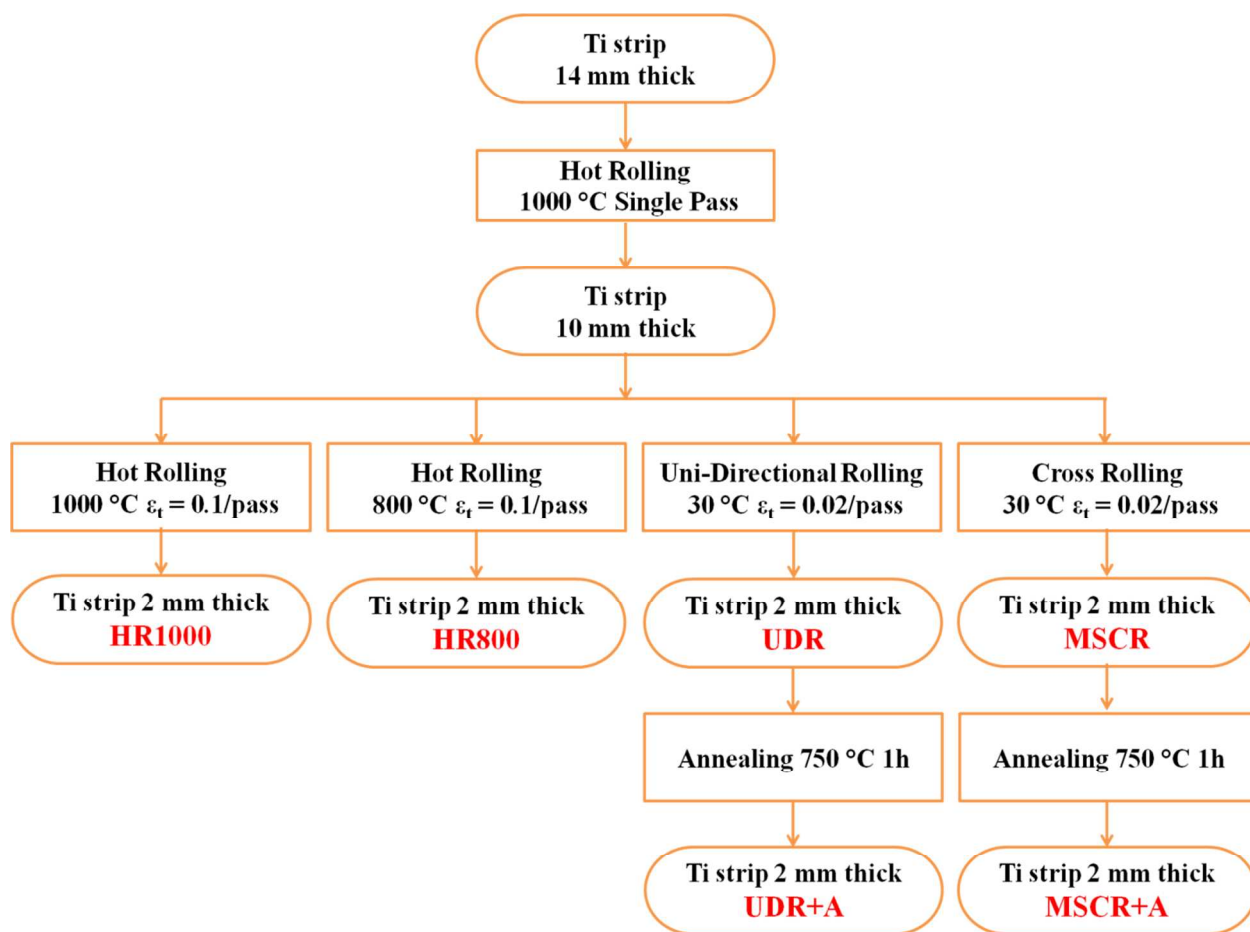


Figure 2

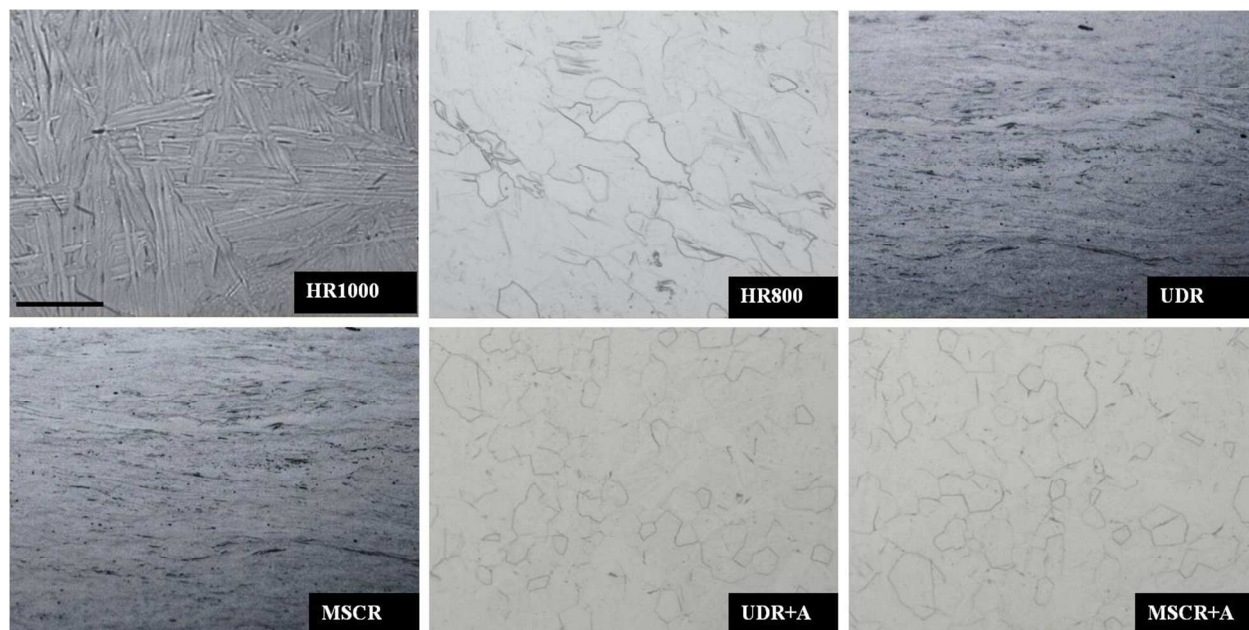


Figure 3

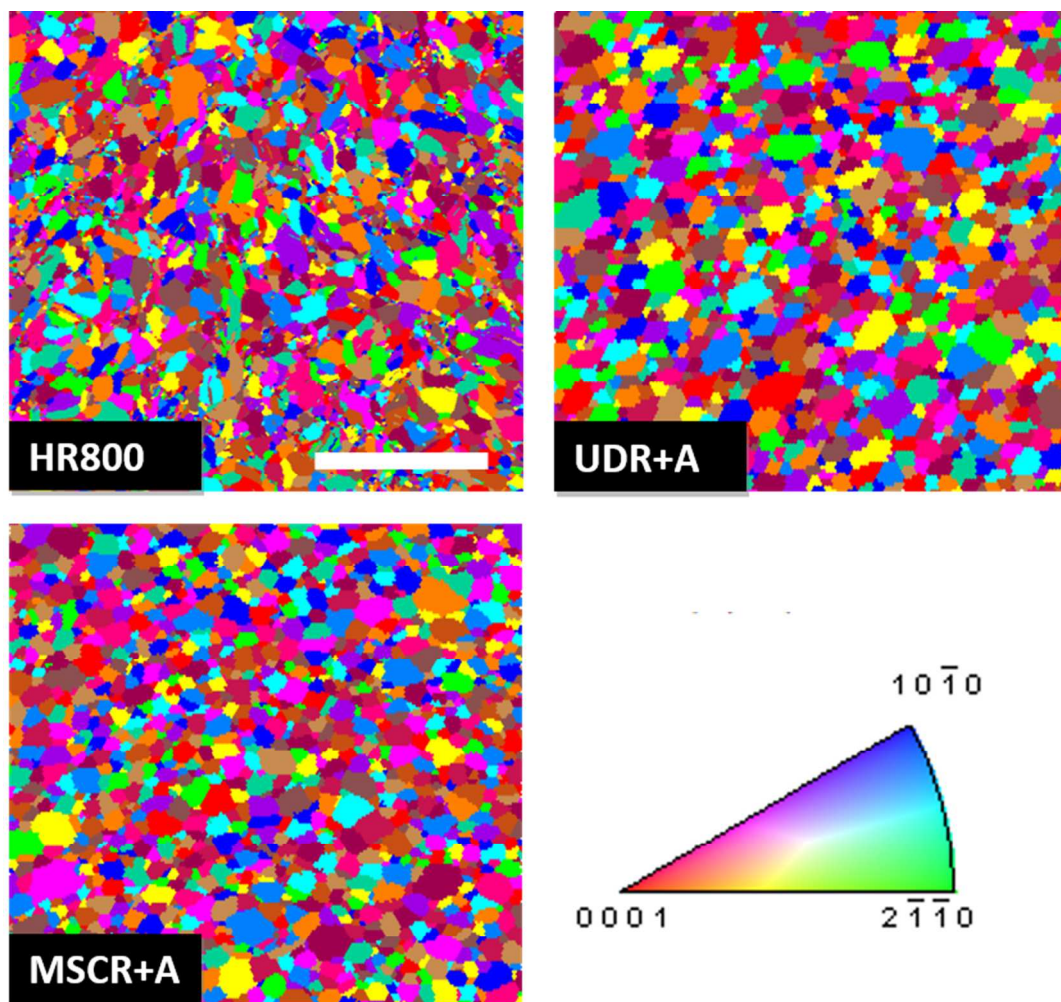


Figure 4

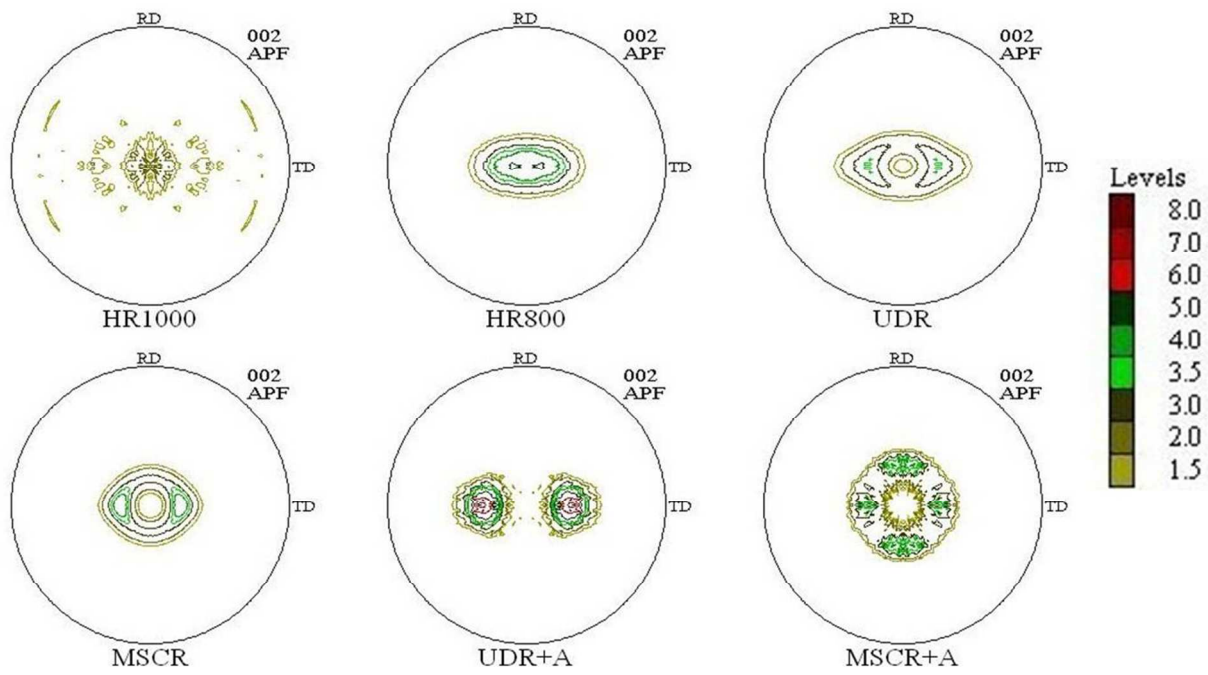


Figure 5

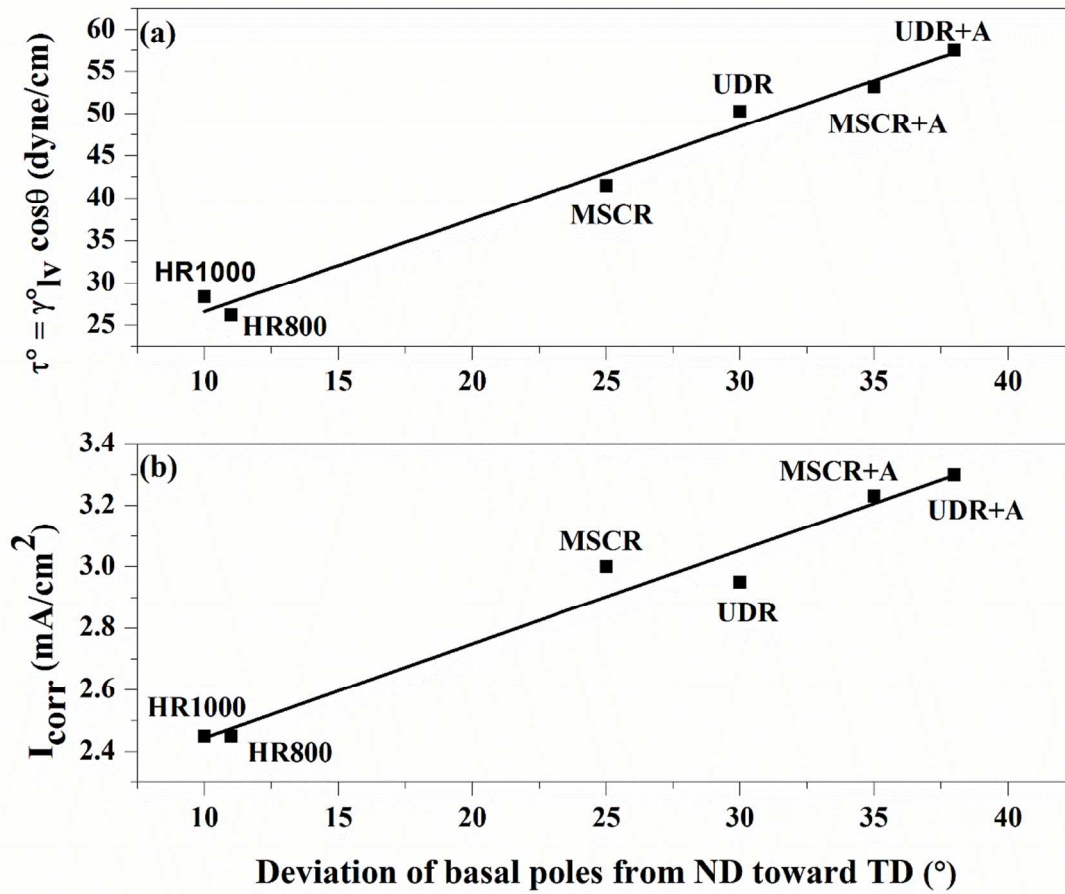


Figure 6

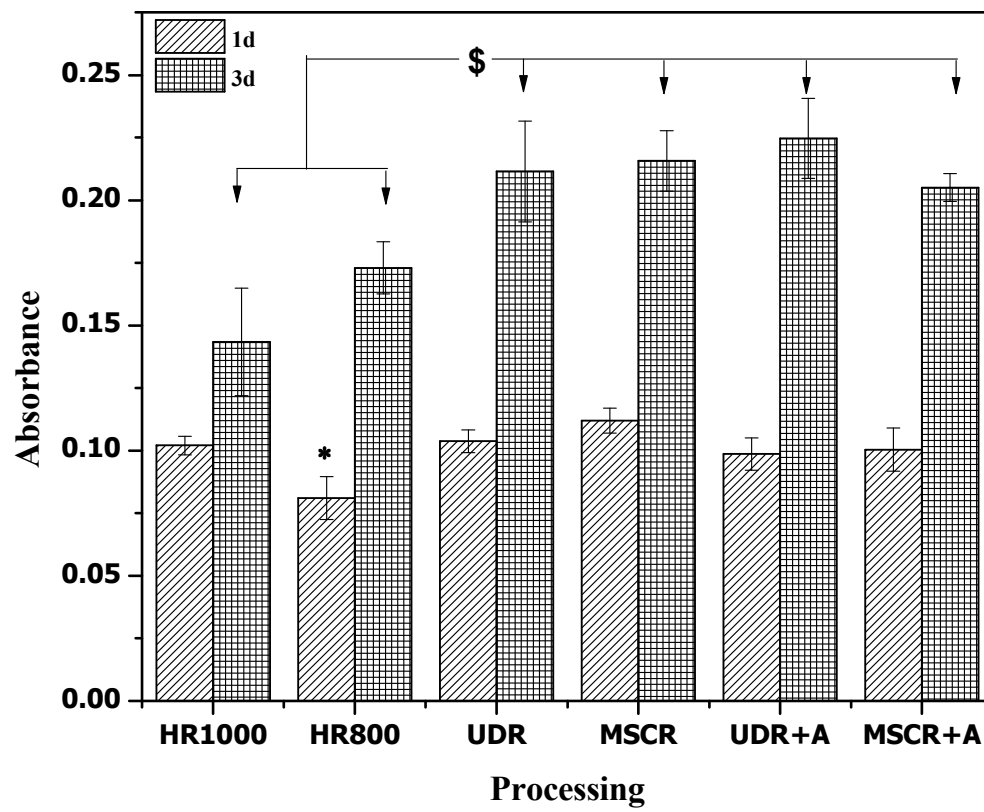


Figure 7

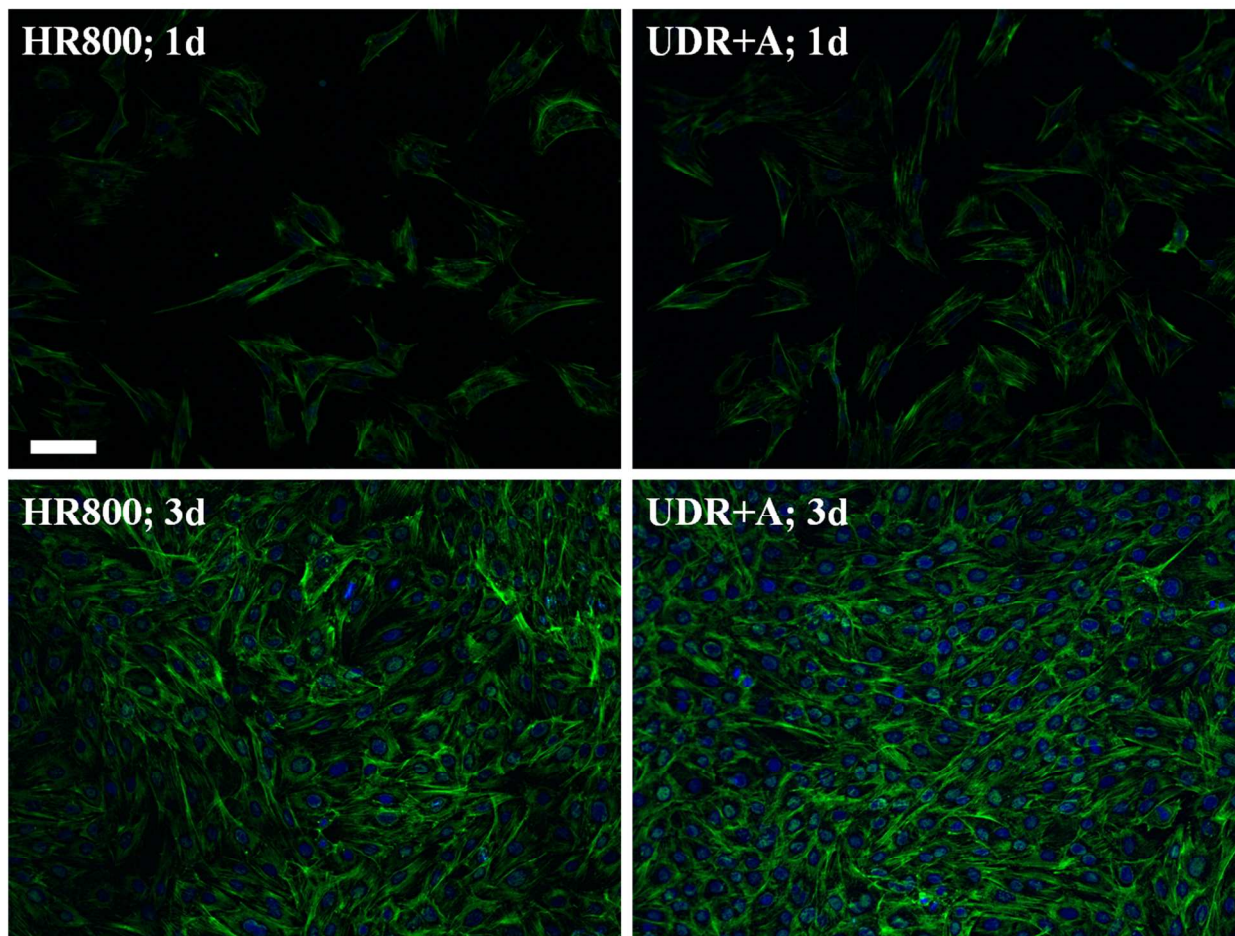
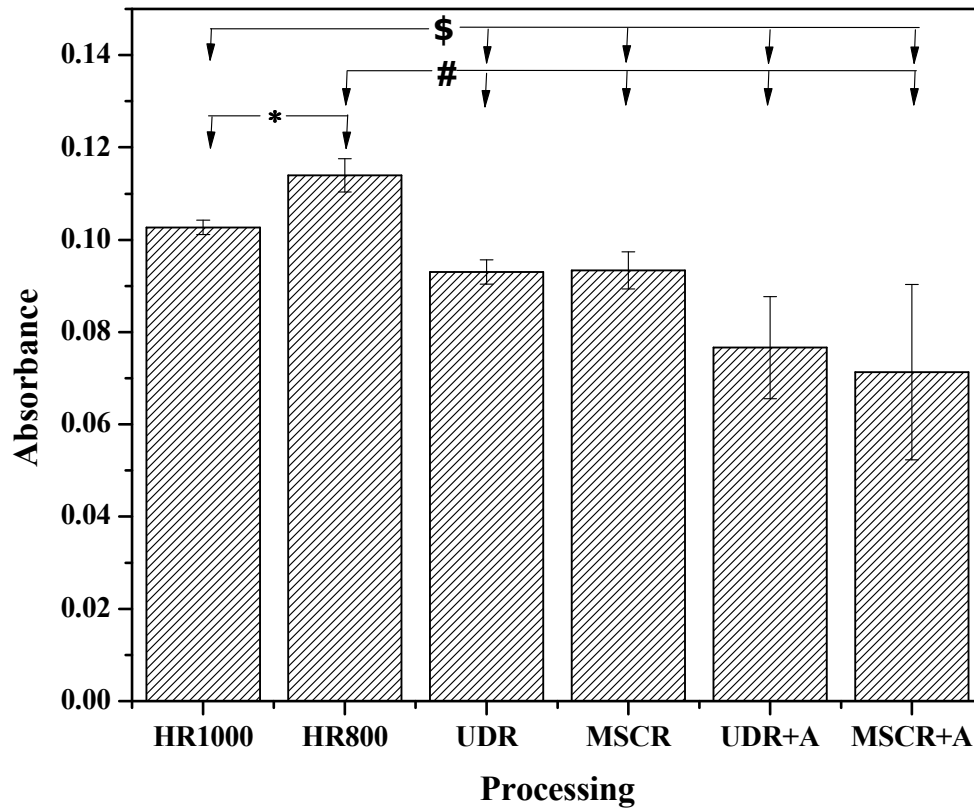


Figure 8



Supplementary Information for
The Importance of Crystallographic Texture in the Use of
Titanium as an Orthopedic Biomaterial

Sumit Bahl, Satyam Suwas, Kaushik Chatterjee*

Department of Materials Engineering, Indian Institute of Science, Bangalore, India 560012

Figure S1

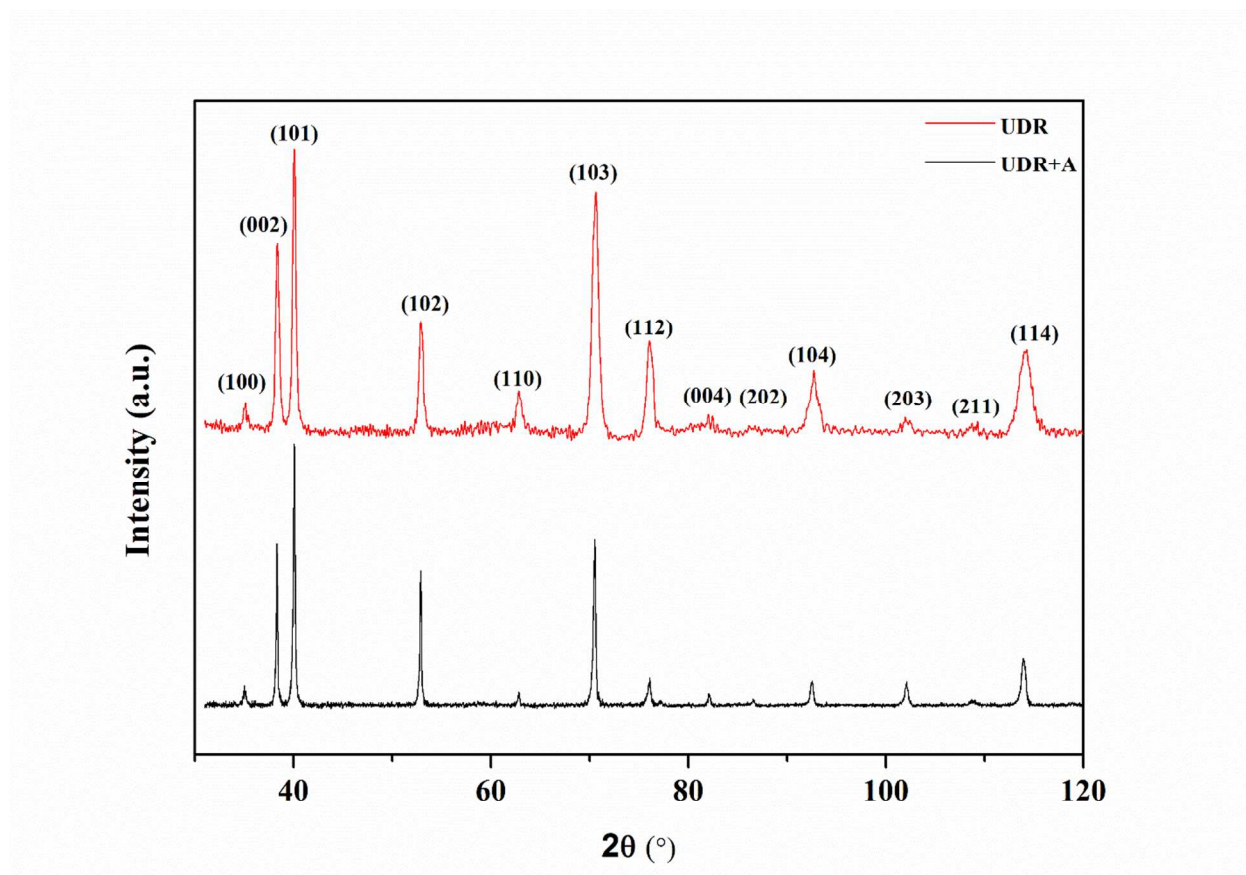


Figure S1. XRD profiles of UDR and UDR+A samples

Figure S2

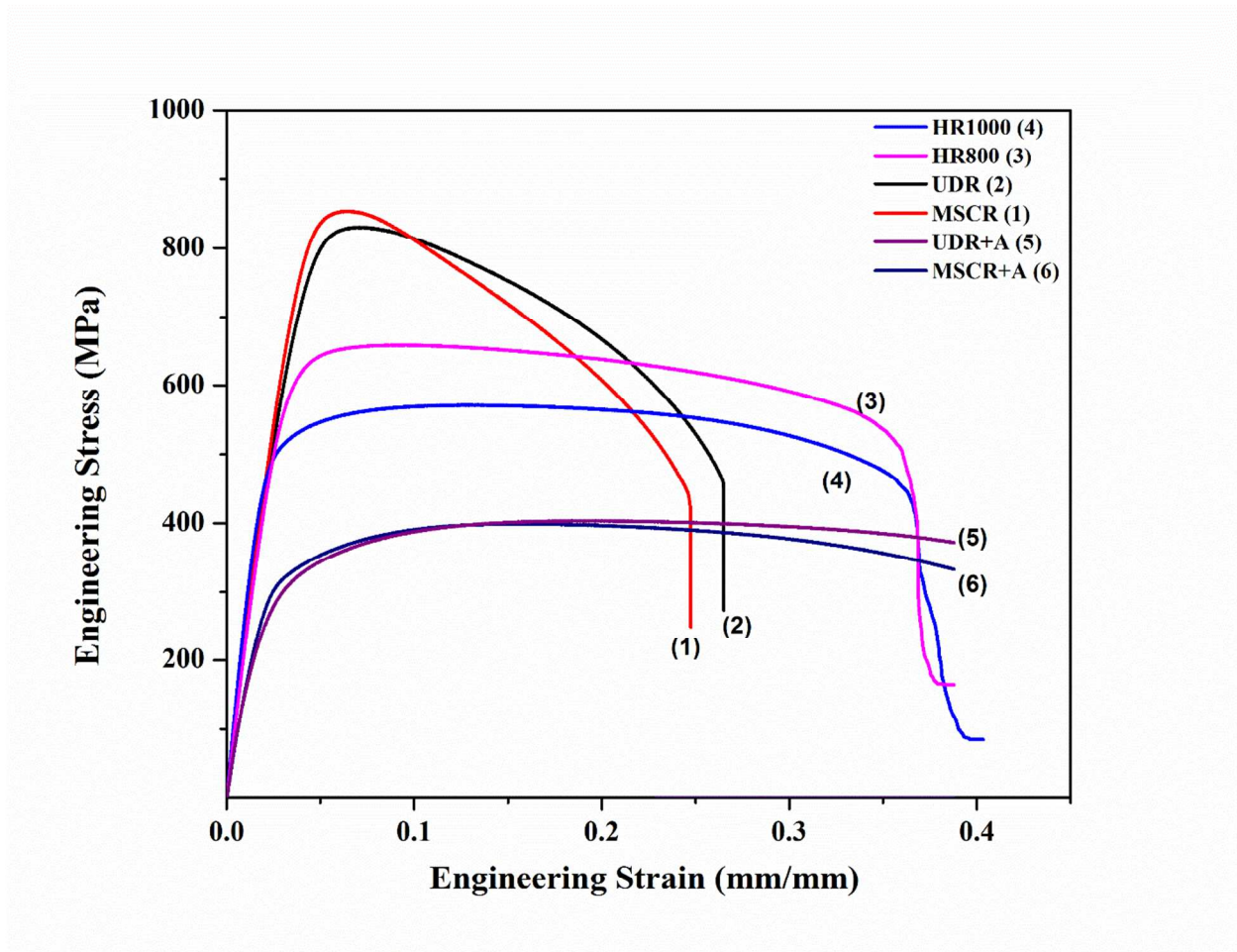


Figure S2. Plots for tensile tests of the different cp-Ti samples.

Figure S3

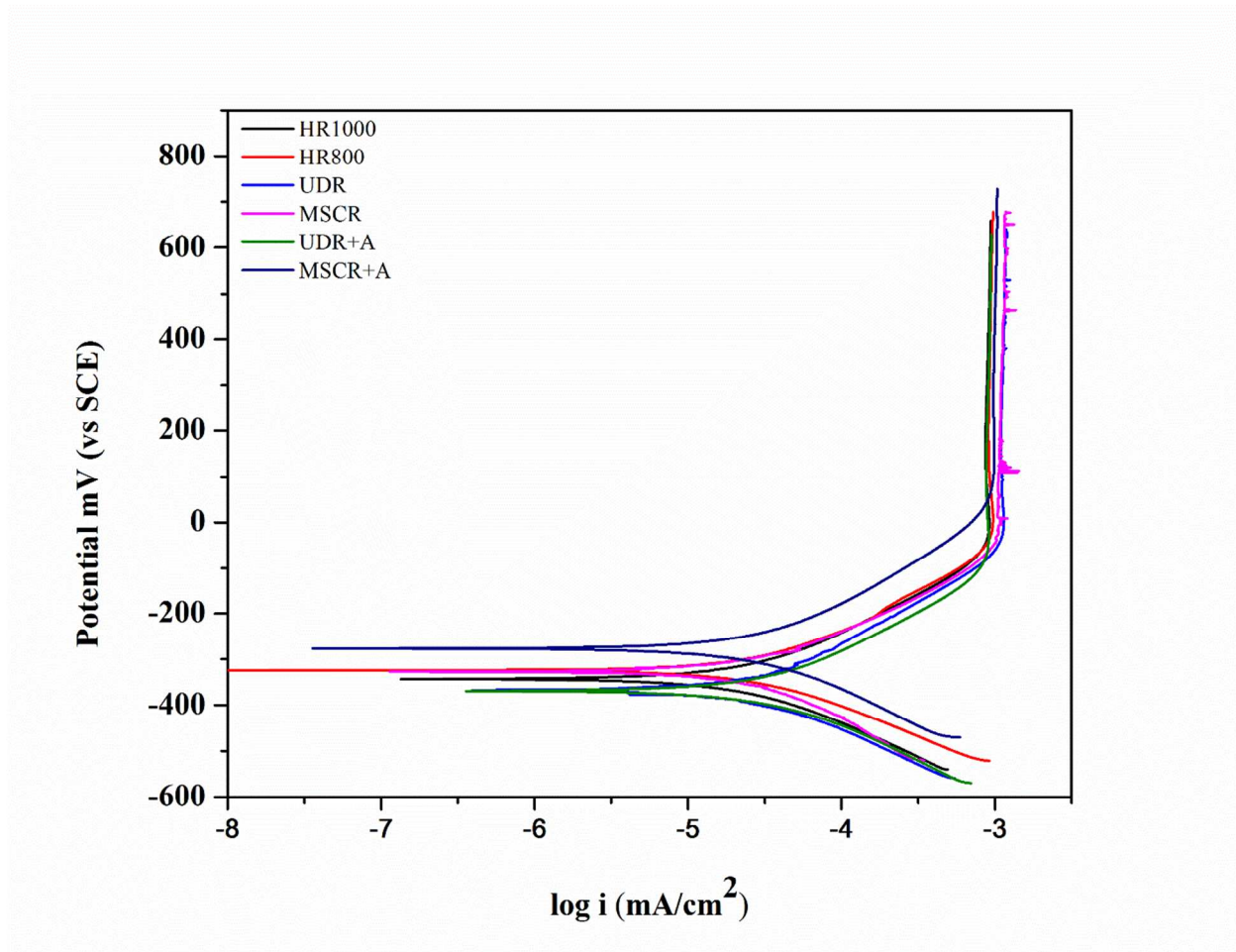


Figure S3. Potentiodynamic polarization plots of cp-Ti samples measured in SBF.

Figure S4

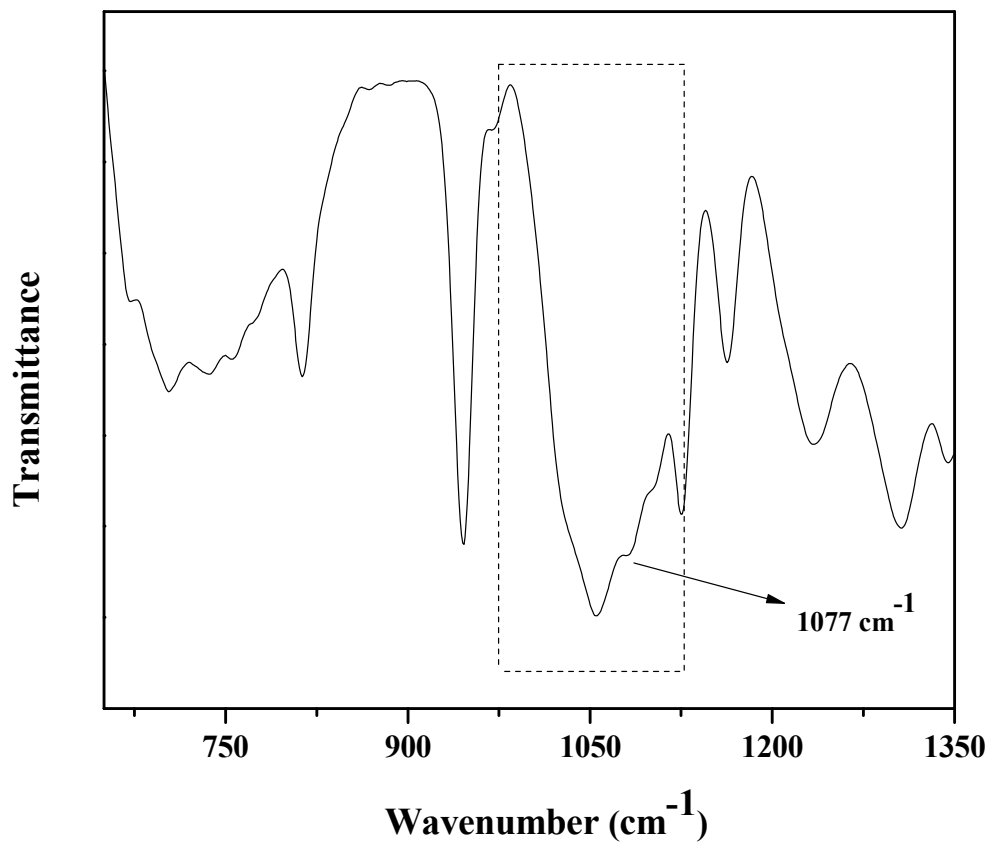


Figure S4. Representative FTIR spectrum of MSCR surface with calcium phosphate mineral deposits.